The final publication is available at

https://doi.org/10.1109/TAP.2021.3137376

Additional Information

High-Efficiency Ka-band Circularly-Polarized Radial-Line Slot Array Antenna on a Bed of Nails

Jose I. Herranz-Herruzo, *Member, IEEE*, Alejandro Valero-Nogueira, *Senior Member, IEEE*, Miguel Ferrando-Rocher, *Member, IEEE*, and Bernardo Bernardo-Clemente

Abstract—Radial-line slot-array antennas (RLSA) provide a extremely simple solution to achieve high-gain circularly-polarized radiation patterns without the need for complicated feeding networks or polarizers. The dielectric-filled radial waveguide, however, drastically reduces the efficiency that is potentially achievable by RLSA antennas at millimeter-wave band. In this paper, a novel architecture for an all-metal RLSA is proposed by replacing the dielectric material with a regular bed of metallic nails, thus maintaining the required slow-wave characteristic within the radial waveguide. The slot array is efficiently optimized by using an adhoc method-of-moments solver, based on the definition of an equivalent problem in the waveguide region. This accurate optimization process, along with the all-metal nature of the antenna, allows to reach a measured peak total efficiency above 80% at 30 GHz. The fabricated prototype consists of two pieces, the bottom waveguide with the bed of nails, and the top slotted plate, which are easily assembled by means of a few screws. Experimental results report a peak gain of 35.0 dBi for a radiation efficiency of 94%, and a wideband matching performance with a very pure axial ratio, below 0.6 dB.

Index Terms—Antenna arrays, circular polarization, slotted waveguide arrays, RLSA, SATCOM, Ka-band, bed of nails.

I. INTRODUCTION

MILLIMETER-wave communication systems promise to provide globally-available broadband services by converging mobile and satellite networks. High data-rate wireless links supporting such systems call for high-gain antennas to compensate for the severe propagation losses at these frequency bands. The use of circular polarization (CP) is also a common specification to avoid an undesirable polarization mismatch in on-the-move communications.

A large variety of mm-wave circularly-polarized arrays have been proposed in the last decade with the aim of replacing the bulky parabolic dishes. These low-profile antennas facilitate their installation and enable an easier satellite tracking on moving platforms. Such arrays usually make use of intricate multilayer corporate-feed networks for a wideband operation, either using metallic hollow waveguides [1]–[3] or printed technologies [4]–[6].

Conversely, an extremely simple approach to achieve a CP high-directive beam without resorting to complicated feeding networks is proposed by the kind of antennas known as radial-line slot arrays (RLSA) [7]. In its more convenient single-
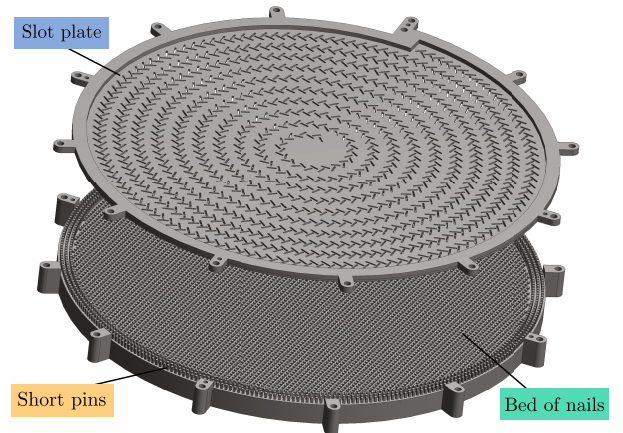
Fig. 1. Exploded view of the all-metal RLSA with a bed of nails.

layer version [8], the cylindrical TEM mode launched by a simple coaxial probe within a parallel-plate waveguide (PPW) excites a large number of rectangular slots, properly arranged for an in-phase broadside CP radiation. These antennas were successfully developed for Ku-band broadcast services, being very attractive due to their structural simplicity, low profile, very good axial ratio and high efficiency when compared to conventional printed arrays. The main drawback of RLSA antennas, however, lies in the well-known trade-off of series-fed arrays between radiation bandwidth and antenna size. In recent years, RLSA antennas have again attracted the attention of researchers, who have proposed new designs for performance improvement [9], [10] or their extension to new applications [11]–[13].

As in other series arrays, the feeding PPW waveguide in an RLSA must be filled with a dielectric material to avoid grating lobes. Despite this fact, RLSA antennas were able to attain a remarkable total efficiency up to 85% in Ku-band [8], [14], supported by a proper slot design. In millimeter-wave band, however, the original RLSA conception barely reaches an efficiency of 50% due to the severe dielectric losses [15].

In this context, several all-metal RLSA realizations have been proposed to improve the radiation efficiency. The absence of dielectric brings additional benefits like an enhanced structural robustness or its potential use in space and high-power applications. In addition, the permittivity uncertainty of dielectric materials often leads to a frequency shift, being an all-metal antenna more reliable at the expense of a generally higher fabrication cost.

In order to keep grating lobes out of the RLSA radiation patterns, the dielectric material must be replaced by an alternative metallic slow-wave structure within the PPW. Concentric circular corrugations were used in [16], [17] to properly shorten the guided wavelength. In this case, a more complex double-layer architecture was adopted, placing corrugations at the upper level. Grating lobes were suppressed satisfactorily in these works, targeting X-band high-power microwave (HPM) applications. Recently, an all-metal K-band single-layer RLSA without slow-wave structure was proposed in [18]. In this work, grating lobes were avoided by reducing slot spacing slightly below the free-space wavelength. Despite being a very simple all-metal low-loss antenna, the in-phase radiation condition is not completely met, and the aperture efficiency decreases with respect to original dielectric-filled RLSAs.

In this paper, a novel all-metal Ka-band single-layer RLSA is proposed, designed and experimentally tested. As can be seen in Fig. 1, a regular pattern of rectangular pins on the lower PPW plate plays the role of the slow-wave structure. This kind of metasurface in a PPW environment has already been used to control the propagation constant in lens design [19], [20]. Here, a bed of identical nails, sufficiently dense to emulate the homogeneous dielectric-filled PPW, has been adopted. As it will be demonstrated in this work, those metallic nails sacrifice some of the RLSA fabrication simplicity in exchange for an enhanced aperture efficiency at mm-wave band.

As it has been repeatedly demonstrated in the past, achieving a highly directive RLSA requires a fine optimization of the theoretical slot arrangement, supported by an accurate characterization of waveguide slot coupling [8], [13], [21]–[23]. Here, an inhouse full-wave method-of-moments (MoM) code has been used to optimize the antenna layout with the aim of maximizing the aperture efficiency. An equivalent model of the PPW with the bed of nails has been defined and validated, thus enabling a fast and accurate optimization process. The all-metal property of the antenna, together with an optimized illumination of array elements, yields a remarkable total efficiency compared to previous mm-wave RLSA.

The rest of the paper is organized as follows. Section II describes the conventional RLSA architecture and gives an overview of its optimization process. In Section III the field propagation along the all-metal PPW with the bed of nails is studied and an equivalent MoM problem is defined and assessed. The developed MoM analysis tool is used in Section IV to design the all-metal RLSA, and the experimental results of a fabricated prototype are reported in Section V. Finally, Section VI draws the main conclusions of this work.

II. RLSA WITH A HOMOGENEOUS PPW

A. Antenna description

As an evolution of the former concept of a double-layer RLSA [7], the single-layer CP-RLSA [8] embraces a very simple structure, depicted in Fig. 2. A homogeneous dielectric-filled PPW, fed at its center by a coaxial probe, constitutes the radial line through which a cylindrical TEM mode propagates outwardly. In order to avoid the propagation of higher-order modes and to ensure a proper array operation, the waveguide height h must be less than half wavelength [7].
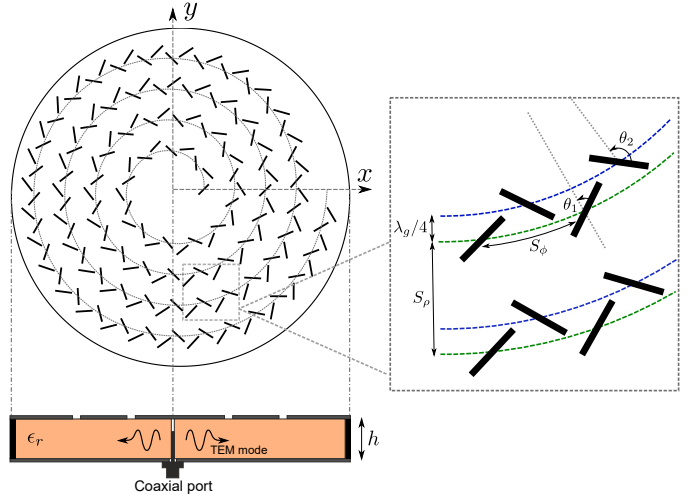

Fig. 2. Schematic of a CP-RLSA and zoomed view of slot pairs.

The basic cell for a broadside CP radiation is formed by two rectangular slots excited in quadrature, for which they must be spaced $\lambda_g/4$ along the radial direction, being λ_g the PPW guided wavelength. Both slots must be equally excited by the TEM mode, so their orientations with respect to the radial direction are defined as $\theta_1 = \pi/4$ and $\theta_2 = 3\pi/4$ (see Fig. 2). The complete RLSA is then formed by repetitions of such slot pair along a counterclockwise spiral for a coherent boresight RHCP radiation. This latter condition also forces the spiral arrangement to be centered at the probe location with a period S_ρ equal to λ_g, whereas the angular array spacing S_ϕ can be freely chosen.

The whole array thus described, often comprising hundreds or thousands of slots, operates as a traveling-wave array. Hence, the TEM wave launched by the probe is progressively radiated through the slots until a small fraction of power reaches the end of the array. For that reason, the edge of the radial guide can be left open, filled with an absorber or ended by a shortcircuit. This latter option is preferable to maximize the radiation efficiency. Note that the described RLSA corresponds to the conventional version, where a spiral slot arrangement is fed by a cylindrical TEM mode. A concentric-array RLSA [14], conversely, arranges slots in circular rings and illuminates them by a spiral mode. Despite attaining an enhanced field uniformity, this version requires a more complex feeding network to generate the rotating mode. In this work, the former spiral RLSA is chosen due to its fabrication simplicity, and an accurate optimization process is carried out to restore a uniform slot excitation.

B. Antenna design and optimization

The RLSA design and optimization followed in this work relies on an inhouse full-wave MoM analysis code, developed by the authors and used in previous works [21], [22]. The MoM analysis makes use of entire-domain sinusoidal basis functions on each slot, which provide a rigorous and fast characterization of the entire RLSA without a huge computational burden. It is worth noting that the fine optimization process here applied
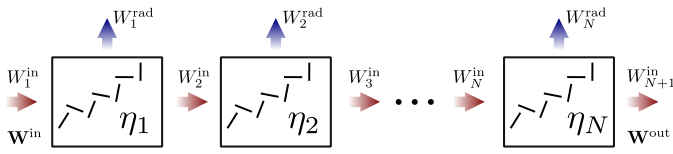
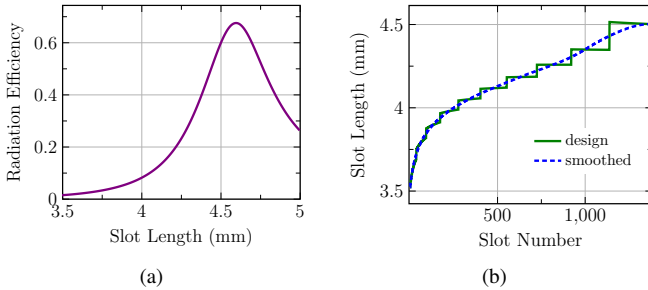Fig. 3. Schematic of the efficiency design in a RLSA.

Fig. 4. (a) Radiation efficiency of one RLSA slot turn versus slot length, and (b) designed slot lengths for a 10-turn RLSA targeting uniform illumination and 5% residual power.

would be very cumbersome if a general-purpose simulation software were used. In previous works, this numerical code demonstrated its accuracy when dealing with RLSA antennas formed by thousands of slots [21], [22].

In this section, a RLSA filled with a homogeneous dielectric will be considered. The described optimization process, though, will remain unaltered when applied to the all-metal antenna proposed below. Once the structural RLSA parameters are chosen, i.e. guide height, h, and permittivity, ϵ_r, slots' width, w, and thickness, t, angular spacing, S_ϕ, and number of spiral turns, N, slots are arranged following the layout shown in Fig. 2. Slots' lengths are established with the goal of achieving a uniform excitation by applying a classical traveling-wave design, depicted in Fig. 3. Given the residual power W_{out}/W_{in} and the desired amplitude distribution, in this case uniform, the radiation efficiency, η_i, of each slot turn is easily computed, which in turn yields the slot length profile across the whole aperture.

For the sake of illustration, a 10-turn RLSA at 30 GHz is considered, with parameters: $h = 4$ mm, $\epsilon_r = 1.2$, $w = 0.8$ mm, $t = 1$ mm, and $S_\phi = 0.5\lambda_0$. Fig. 4(a) plots the fundamental design curve relating the radiation efficiency and the slot length. More details about the computation of this correspondence will be given in Section III. A uniform aperture with a residual power of 5% is designed, resulting in 1376 slots whose lengths are plotted in Fig. 4(b), sorted by radial distance. As it is known, increasingly longer slots are required to compensate for the natural decay of the cylindrical TEM mode and the gradual slot radiation. As seen in Fig. 4(b), the discrete design results in a step in slot length when a new spiral turn begins. In order to improve the field uniformity, a smoothed length profile has been chosen in this work, also plotted in Fig. 4(b).

As it has been pointed out in previous works [8], [13], [21]–[23], the presence of slots markedly perturbs the propagation constant of the TEM mode within the PPW, spoiling the phase uniformity of the excitation of the slots themselves, and hence
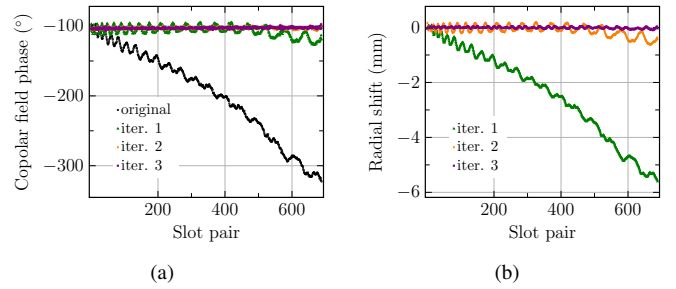

Fig. 5. Iterative optimization procedure of a 10-turn RLSA: (a) phase of the copolar radiated field and (b) radial shift of each slot pair.

considerably reducing the directivity. Keeping in mind the working principle of the RLSA antenna, the desired in-phase array excitation can be easily restored by shifting the position of each slot pair in the radial direction [21], [22]. Theoretically, the shift of the i-th pair should follow the expression:

$$\Delta\rho_i = \frac{2\pi}{\lambda_g}\Delta\alpha_i \tag{1}$$

where $\Delta\alpha_i$ is the phase error of the i-th slot pair to be corrected. In this case, such error is computed taking the first slot pair as the common reference, i.e. $\Delta\alpha_i = \alpha_i - \alpha_1$. This choice allows to keep the initial position of the RLSA spiral fixed. The value α_i corresponds to the phase of the copolar RHCP field radiated by the i-th slot pair in the broadside direction. Note that this magnitude can be easily computed by the dedicated MoM model of the RLSA problem, unlike the finite-element method widely used by general-purpose simulation software.

The correction given by (1) is performed iteratively until convergence is reached, giving as a result the optimized RLSA aperture. The convergence and effectiveness of this procedure is demonstrated in Fig. 5(a) by plotting the phase of the broadside copolar field radiated by each slot pair for the case under study. With the original slot layout, the excitation phase decreases steadily as the wave propagates within the radial guide. Such phase error is largely corrected by the first iteration, except for a small phase ripple and a slight decay at the outer slots. Then, the second iteration almost completely restores the desired uniform phase profile, reaching convergence with a third iteration.

The radial shift of each slot pair is represented in Fig. 5(b) for the three iterations performed. As expected, the displacement given by the third iteration is negligible and, therefore, the optimization procedure is terminated. This graph reveals that the outermost slots are shifted around 6 mm, beyond half wavelength, due to the fact that the original slot layout shows a maximum phase error above 200º. Hence, originally, the innermost and the outermost slots are radiating an out-of-phase copolar component, reducing dramatically the antenna directivity.

A helpful visualization of the optimized slot excitation is shown in Fig. 6, where the aperture field is represented. The bi-dimensional graphs (Figs. 6(a) and 6(b)) provide an immediate overview of the array illumination, while the one-dimensional
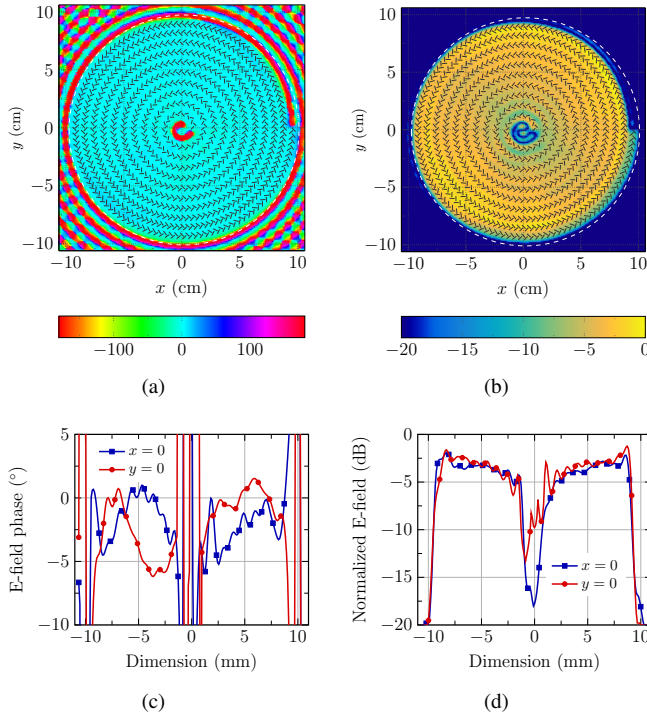
(a)

(b)

(c)

(d)

Fig. 6. Copolar component of the electric field across the 10-turn RLSA aperture: 2D representation (above) and 1D cuts along $x = 0$ and $y = 0$ planes (below). The phase is represented in degrees (left) while the normalized magnitude is plotted in dB (right).

(a)

(b)

Fig. 7. Copolar radiation pattern of a 10-turn RLSA at 30 GHz: (a) before and (b) after optimization.

TABLE I
10-TURN RLSA ANTENNA PARAMETERS

	AR (dB)	SLL (dB)	D_{max} (dBi)	η_{rad} (%)	η_{ap} (%)	η_{tot} (%)	HPBW (°)
Original	0.04	-10.5	29.92	96.2	24.4	23.5	3.38
Optimization	0.06	-14.6	35.15	97.4	91.1	88.7	2.99
Shortcircuit	0.32	-14.7	35.07	100	89.4	89.4	2.99

Antenna parameters of a 10-turn RLSA for the first theoretical design, the optimized arrangement, and the latter with a final shortcircuit.

cuts shown in Figs. 6(c) and 6(d) allow a more precise reading. Neglecting the central slot-free area, a satisfactory field uniformity is achieved across the entire aperture, particularly good for the optimized phase component, as expected.

In this regard, Figs. 6(b) and 6(d) reveal that innermost slots present a slightly smaller excitation due to the finite array effect. Because of this same reason, the outermost slots exhibit a stronger excitation. Such differences, however, have a minor impact on the overall radiation performance and an optimum aperture efficiency is achieved, as shown below. Note that the correction procedure could also have optimized the slots' lengths to pursue a completely uniform amplitude distribution. However, it has been found that such slot length tuning has a minor impact on the radiation pattern and often compromises the process convergence. For these reasons, the phase-only correction procedure described above was adopted here.

The radiation patterns at the design frequency for the original and the corrected antenna are shown in Fig. 7. It is evident how the low-directive pattern provided by the original RLSA arrangement, shown in Fig. 7(a), is drastically enhanced after the optimization process, leading to a narrow well-shaped broadside main beam in Fig. 7(b). Note that radiation patterns are nearly identical along both planes despite the intrinsic asymmetry of the spiral slot arrangement. The most relevant antenna parameters at 30 GHz are reported in Table I, comparing the original and the optimized RLSAs. As it can be noted, the optimization routine is capable of improving the aperture efficiency from a poor value of 24% to a remarkable 91%. Conversely, axial ratio in both cases is below 0.1 dB,
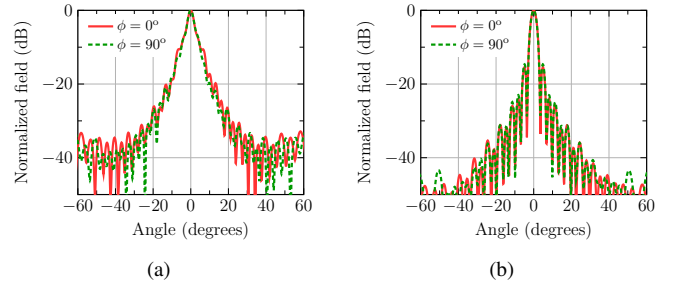
confirming the good polarization properties of RLSA antennas, and radiation efficiency is quite close to the design goal of 95%. Lastly, Table I also includes the optimized RLSA when a final circular shortcircuit is added. The position of such metallic cylinder is shown in dashed white line in Fig. 6(b). Among other practical advantages, the shortcircuit enables to radiate the whole input power (ohmic losses are not considered in MoM analysis), at the expense of a worse axial ratio. This latter fact will be addressed in Section IV.

One additional aspect in RLSA design, particularly relevant in this work, is the antenna performance for low-permittivity radial waveguides. As it will be seen in next section, the slow-wave property of the dielectric material will be implemented by an all-metal bed of nails, whose behavior improves for lower synthesized permittivities. In this regard, the aperture efficiency of the 10-turn RLSA is represented versus the chosen ϵ_r in Fig. 8(a). As expected, when the PPW is filled with air, the presence of grating lobes leads to a lower antenna directivity. Note that the optimized RLSA tends to bring slots closer, thus reducing the endfire radiation, as seen in Fig. 8(b). Beyond a certain value of PPW permittivity, the aperture efficiency reaches an optimum value thanks to the absence of grating lobes. By inspecting the curves in Fig. 8, a permittivity value of 1.15 seems enough to guarantee a good radiation performance within a wide frequency band.

III. PPW WITH A BED OF NAILS

The all-metal RLSA antenna proposed here replaces the dielectric within the radial guide by a periodic bed of metallic pins (see Fig. 1). As seen above, a simple air-filled PPW is not capable to support a highly directive RLSA, needing to resort to a slow-wave medium within the waveguide. In this section, the properties of an all-metal PPW with a bed of nails are first studied, leaving the RLSA design for the next section.
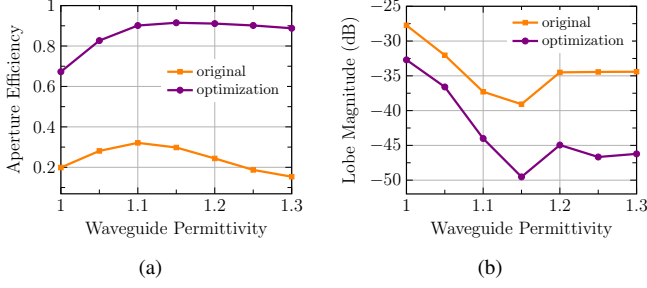
Fig. 8. Study of the PPW permittivity variation in a 10-turn RLSA: (a) aperture efficiency, and (b) magnitude of the endfire radiation.
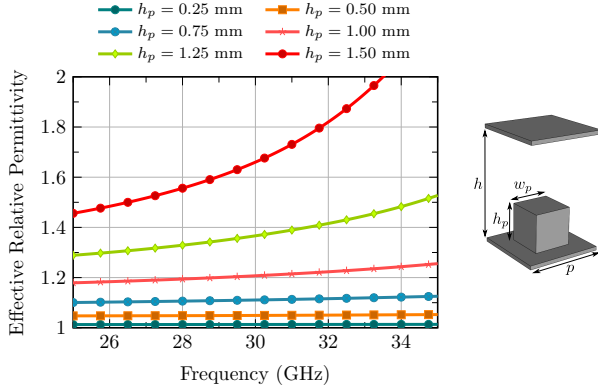

Fig. 9. Effective relative permittivity of a PPW with a bed of nails: w_p = 1 mm, h = 4 mm, p = 2 mm.

Fig. 10. Instantaneous E_z component within a PPW with a bed of nails: (a) pins layout and source position (in red); (b) top view; (c) side view.

Fig. 11. H_ϕ component on the top plate of a PPW with a bed of nails, along circumferences of growing radii: (a) magnitude and (b) phase.

Firstly, the propagation constant of the fundamental mode within the PPW with the bed of square-section nails is evaluated. The periodic cell under study is depicted in Fig. 9 with all its relevant dimensions. Pin periodicity, p, and width, w_p, are 2 mm and 1 mm respectively, and the total guide height, h, is 4 mm. The curves in Fig. 9 represent the effective relative permittivity versus frequency for different pin heights h_p, computed as:

$$\sqrt{\epsilon_{r,ef}} = \frac{\lambda_0}{2\pi}\beta \qquad (2)$$

where β is the propagation constant of the fundamental mode given by the eigenmode solver in CST Studio suite [24]. Predictably, higher pins introduce a more noticeable perturbation of wave propagation, leading to a higher effective permittivity. Likewise, shorter pins provide a more stable permittivity in terms of frequency. This coherent behavior makes it advisable to choose pins as short as possible to maximize the structure bandwidth. In this case, a pin height h_p = 0.87 mm is adopted hereinafter to synthesize the value $\epsilon_{r,ef}$ = 1.15 chosen in previous section.

For the sake of design simplicity and fabrication ease, pins are arranged along a square grid on the PPW bottom plate. Such arrangement breaks the rotational symmetry of the waveguide and will therefore have an impact on the angular uniformity of the guided wave. To assess this impact, such waveguide is excited by a discrete current source and the instantaneous electric field is represented in Fig. 10(b), sampled on the inner face of the top plate. It can be seen
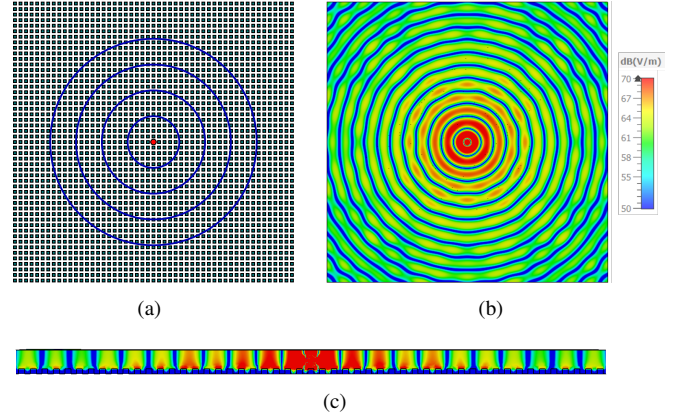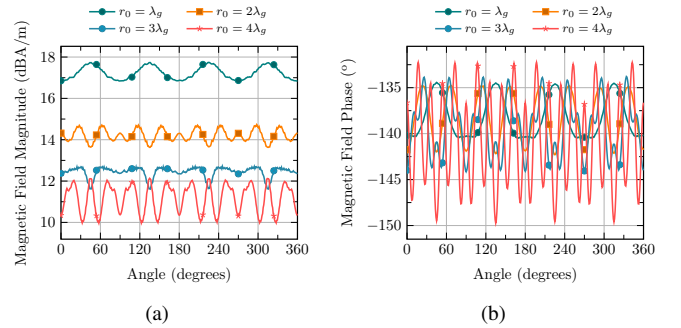
that the guided wave exhibits quasi-cylindrical wavefronts with a reasonably small ripple. In the side cross-section view of Fig. 10(c), it can be seen how the field slightly penetrates the gaps between pins, but it is mostly confined within the air region above them.

A more precise field visualization is shown in Fig. 11, where the azimuthal component of the magnetic field is sampled at integer multiples of the guided wavelength $n\lambda_0/\sqrt{\epsilon_{r,ef}}$ from the source, along the circumferences shown in blue in Fig. 10(a). Despite the field variation strongly depends on the sampled radial distance, the magnitude ripple remains below ± 1 dB and the phase ripple is mostly below $\pm 7°$. As it will be demonstrated later, this behavior is good enough to achieve a highly uniform illumination of the slot array. Note that a more homogeneous field would be achieved for smaller pin periods, but at the cost of increasing the fabrication complexity.

As it was demonstrated above, achieving a highly directive RLSA requires an optimization process supported on an accurate antenna analysis. However, the proposed all-metal PPW with the bed of nails is not well-suited to be analyzed by a dedicated MoM code, and the general-purpose electromagnetic simulators are not efficient enough for an iterative optimization routine. In this work, an equivalent problem has been defined for the waveguide region, more appropriate for a MoM model. This new problem must provide an accurate characterization of the field propagation and the slot coupling within the all-metal
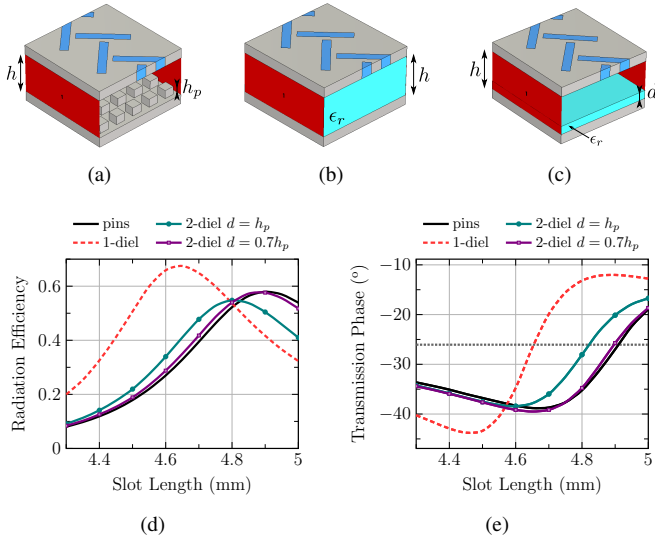
Fig. 12. Slot coupling model: (a) with pins, (b) homogeneous, and (c) partially-filled PPW. (d) Radiation efficiency and (e) phase of the S_{21} transmission coefficient versus slot length.
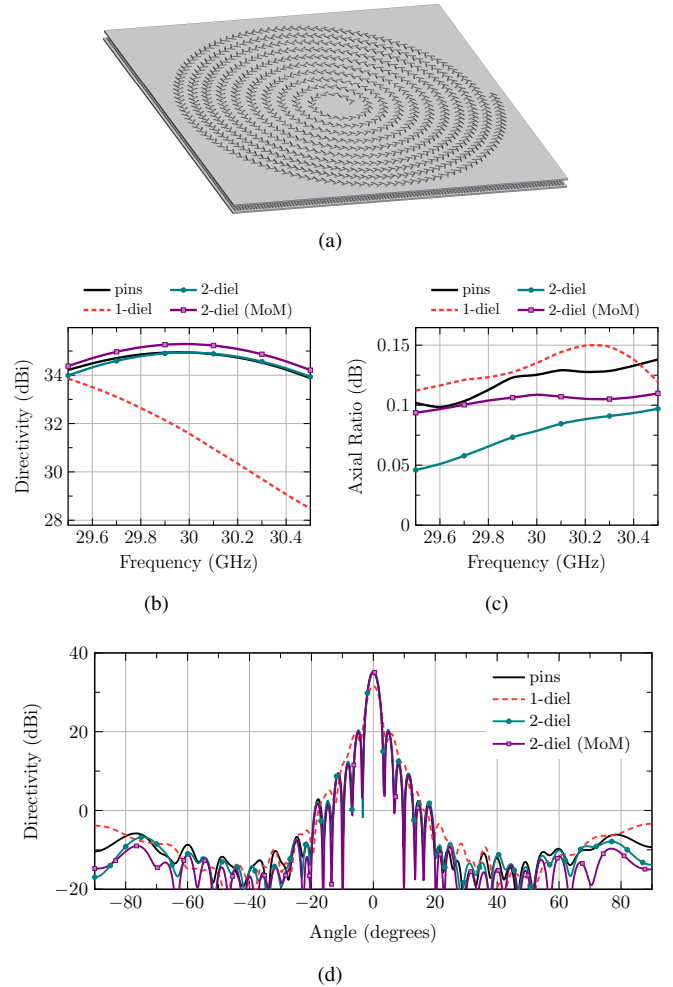

Fig. 13. Antenna parameters of a 10-turn RLSA with a bed of nails, compared to equivalent models: (a) antenna view, (b) maximum directivity, (c) broadside axial ratio, and (d) radiation pattern at 30 GHz along $\phi = 0°$ plane.

PPW. In order to assess such equivalence, a representative structure in RLSA performance has been taken as reference. For the latter, a periodic cell modeling a slot turn, depicted in Fig. 12(a), is simulated with the CST finite-element solver, excited by one TEM port at each side. This periodic structure is used as the reference model to compute the efficiency curve used in RLSA design, described in Section II.

The simplest equivalent problem consists of removing the bed of nails and filling the PPW with an homogeneous dielectric with $\epsilon_r = \epsilon_{r,ef}$, as shown in Fig. 12(b). Two important magnitudes in RLSA design have been evaluated to compare these models: the radiation efficiency (Fig. 12(d)) and the phase of S_{21}-parameter (Fig. 12(e)) versus slot length. It can be seen that the homogeneous PPW model (in dashed red) do not emulate properly the PPW with the bed of nails (in solid black), exhibiting a noticeable shift to shorter slot lengths. This behavior is somewhat expected since in the latter model slots see an air medium beneath them, in contrast to the dielectric-filled PPW.

A more suitable equivalent model is defined in Fig. 12(c). A dielectric sheet is placed on top of the bottom PPW plate, leaving the rest of the PPW filled with air. In this two-dielectric model, the constitutive parameters are adjusted to match the propagation constant of the fundamental mode given by $\epsilon_{r,ef} = 1.15$. As a natural choice, in first place, the total PPW height is fixed to that of the PPW with pins, $h = 4$ mm, whereas the thickness of the dielectric sheet is set equal to the pins height, $d = 0.87$ mm. Then, by solving the known transcendental equation of a partially-filled PPW [25], the permittivity of the dielectric sheet is found to be $\epsilon_r = 1.98$.

This two-dielectric model with $d = h_p$ yields a much better approximation to the pinned PPW, as shown in Fig. 12, though a slight curve shift is still observed. After several trials among the degrees of freedom available, it has been concluded that a very good characterization can be achieved by setting $d = 0.7h_p$, and matching the air thickness $h - d$ to

the distance between pins and the top PPW plate $h - h_p$ in the reference model. In this case, the dielectric sheet permittivity is $\epsilon_r = 2.85$. This modified two-dielectric model now accurately matches the curves given by the pinned PPW, as demonstrated in Fig. 12. Note that this equivalent problem is now well-suited to be analyzed by a dedicated MoM code using the well-known Green's functions of a multilayered PPW.

IV. ALL-METAL RLSA DESIGN

An analysis MoM code has been developed to accurately analyze the entire all-metal RLSA proposed in this work. The tuned two-dielectric equivalent model of previous section has been adopted in the waveguide region. Such tool enables an efficient optimization of the whole slot array by following the same procedure described in Section II for a conventional dielectric-filled RLSA.

The slot layout of the designed 10-turn RLSA is shown in Fig. 13(a), being 19.8 cm in diameter and comprising 1406 slots. The antenna structure keeps the same parameters used in previous sections, namely, $h = 4$ mm, $h_p = 0.87$ mm, $w_p = 1$ mm, $p = 2$ mm, $w = 0.8$ mm, $t = 1$ mm, and $S_\phi = 0.5\lambda_0$. The maximum directivity and the axial ratio are

(a)

(b)

Circular short

Bed of nails

(c)

Spiral short

Bed of nails

(d)
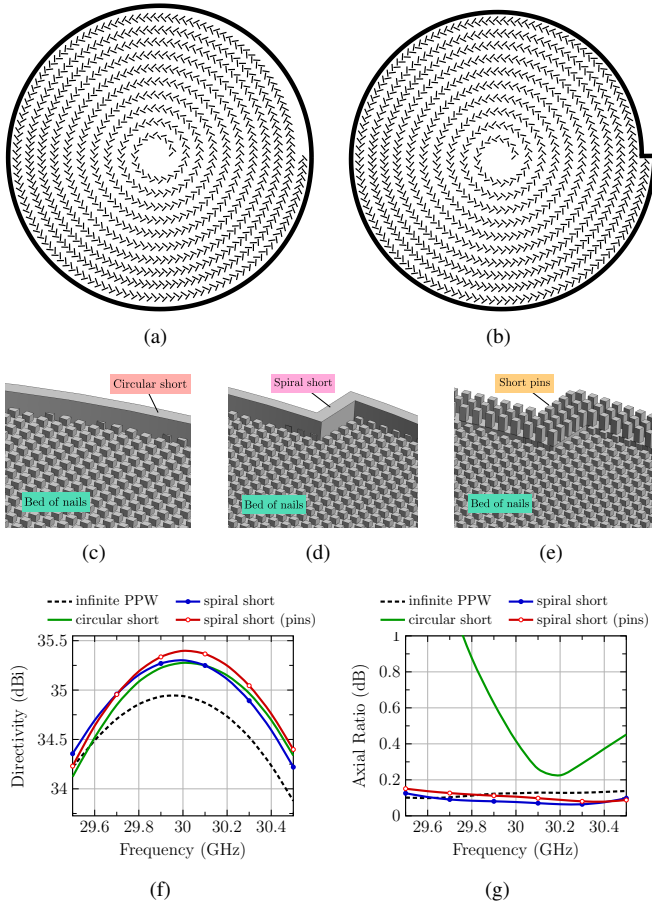

Short pins

Bed of nails

(e)

(f)

(g)

Fig. 14. Different shortcircuit implementations: (a) circular short and (b) spiral short. Detail of the short without the slotted cover: (c) circular short, (d) spiral short, and (e) spiral short implemented by pins. Impact of the shortcircuit on antenna performance: (f) maximum directivity and (g) axial ratio versus frequency.

plotted in Figs. 13(b) and 13(c), respectively. For the sake of illustration, the CST simulation results of the all-metal antenna are compared to those obtained with the homogeneous and two-dielectric PPW models, along with the MoM code.

The directivity curve reveals the good performance of the optimization process, with a peak value of 34.9 dBi at the design frequency. This fact reinforces the estimable accuracy of the two-dielectric model, as shown in Fig. 13(b), in contrast to the unacceptable approximation of the homogeneous PPW model. As for the axial ratio, a very good polarization purity is revealed in the whole frequency band. Lastly, the radiation pattern at the design frequency, plotted in Fig. 13(d), confirms again the precision of the MoM code resulting in an accurate design of a uniform antenna aperture.

Once the slot layout is optimized considering an infinite waveguide, a shortcircuit is added along its outer contour with the aim of radiating the residual power. Its position must be tuned to maximize the directivity and axial ratio, being the optimum distance from the short to the outermost slots around $0.5\lambda_g$. Two different short realizations are considered, circular and spiral-shaped, which are depicted in thick black line in Figs. 14(a) and 14(b) respectively. Note that the spiral shortcircuit keeps a constant distance from the outermost slot
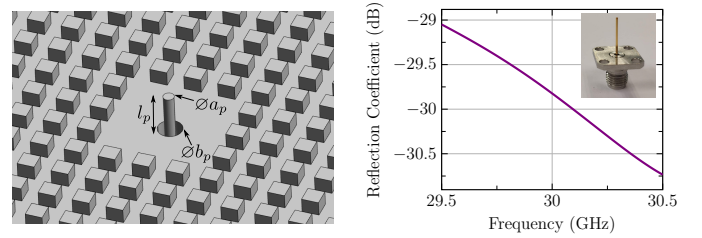

Fig. 15. Reflection coefficient at the coaxial port for an infinite PPW with a bed of nails. The physical connector is shown in the graph inset and the dimensions in the left drawing.

turn, which will be more appropriate to control the phase of the reflected wave. Shortcircuit condition is attained by a wall of a given thickness at the end of the bed of nails, in contact with the top slotted plate. A zoomed view of the practical realization is shown in Figs. 14(c) and 14(d).

Directivity and axial ratio for both short realizations are shown in Figs. 14(f) and 14(g) respectively. It can be observed on the one hand that either option provides a proper directivity curve with a maximum value at the design frequency. Axial ratio, on the other hand, confirms that the spiral-shape short preserves the optimum polarization purity provided by the infinite waveguide design, in contrast to the circular short case. Note that the backward wave reflected from the short is responsible for a crosspolar component.

One critical issue of this all-metal RLSA is how to assure a perfect electrical contact between the short rim and the top slotted plate. Applying a soldering paste or placing a large number of screws could be effective solutions, but any air gap between pieces would lead to field leakage, especially at mm-wave band. In this work, the contactless property of gap waveguide technology [26] has been exploited by replacing the shortcircuit with three rows of nails, as seen in Fig. 14(e). Directivity and axial ratio curves for the designed RLSA with such short pins are also plotted in Figs. 14(f) and 14(g), respectively, revealing a practically identical performance compared to that of the continuous spiral short.

Lastly, once the slot layout and the shortcircuit are defined, the antenna feeding is considered. Note that an ideal current source has been used so far. Here, a coaxial probe is introduced into the all-metal PPW through a circular hole drilled in an square area free of pins. As seen in Fig. 15, three rows and columns of pins are wiped out to leave room for the probe and help matching. Specifically, the coaxial K probe Southwest 1012-24SF, with inner and outer diameters $a_p = 0.635$ mm and $b_p = 1.435$ mm, respectively, is used. By tuning the length of the probe introduced into the PPW, $l_p = 2.27$ mm, a good matching is achieved in a wide bandwidth without requiring a disk-loaded probe, as seen in Fig. 15.

V. EXPERIMENTAL RESULTS

The all-metal RLSA described above is fabricated and validated experimentally. The antenna is constructed in two separate pieces, assembled with screws. As shown schematically in Fig. 16, the bottom piece includes the hole through which the feeding probe is introduced, the bed of nails, and
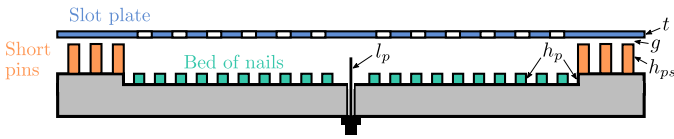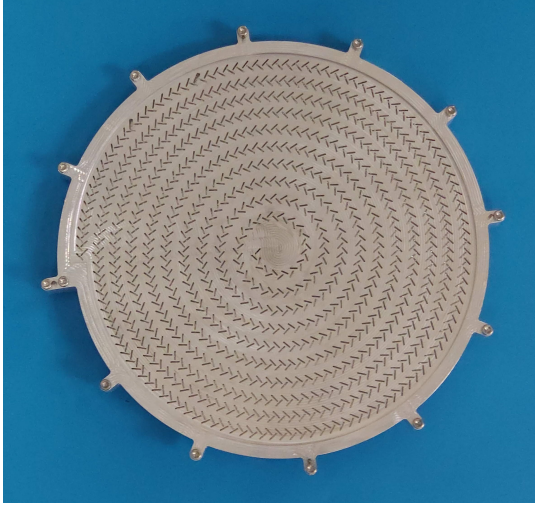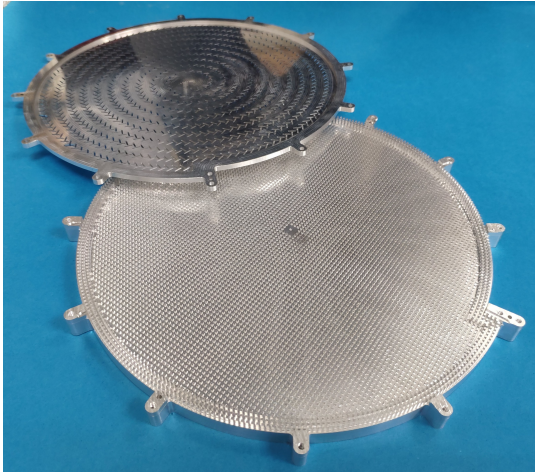
Fig. 16. Side-view schematic of the RLSA showing the different height parameters.

(a)

(b)

Fig. 17. Pictures of the fabricated prototype: (a) top view of the assembled antenna, and (b) view of both parts disassembled.
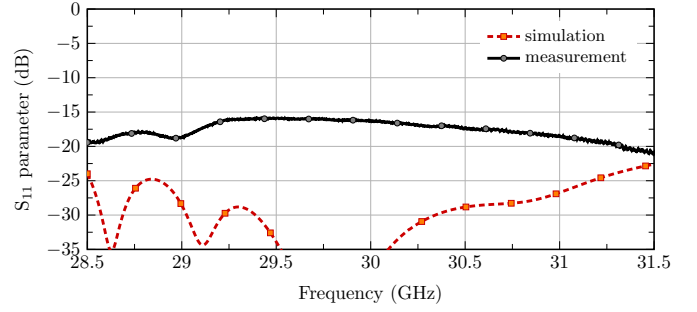

Fig. 18. Measured and simulated reflection coefficient at coaxial input port.
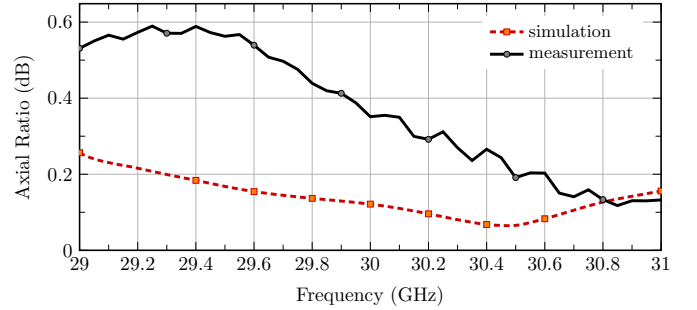
Fig. 19. Measured and simulated boresight axial ratio versus frequency.

a final spiral-shaped pedestal along which the short pins are arranged. Such pedestal has the same height $h_p = 0.87$ mm as the bed of nails, whereas the height of the shortcircuit pins is $h_{ps} = 2.5$ mm to avoid field leakage. The top piece is merely a plate of thickness $t = 1$ mm, where slots are drilled. Both pieces are assembled leaving an air gap $g = 0.63$ mm between the top of the short pins and the slotted plate.

The antenna is fabricated entirely in aluminum by a CNC milling machine. A top view of the constructed antenna and both pieces disassembled are shown in Fig. 17. Twelve screws and four alignment pins are arranged along the outer antenna contour in order to assure a proper assembly of the pieces. Besides that, with the aim of improving the structural robustness of the slotted plate, a thicker spiral rim is added along the edge of this piece. It should be noted that two slots belonging to the outermost spiral turn have been drilled thicker than required due to a CNC manufacturing error, albeit with negligible impact on antenna performance.

The reflection coefficient at the input coaxial port is measured with a vector network analyzer, and plotted in Fig. 18 compared to simulation. An S_{11}-parameter better than -15 dB is measured in a wide frequency band, despite it does not reach the optimum level predicted by simulation. Note that, due to the fact that the slot array is inherently well matched, the antenna matching performance is mainly governed by the coaxial probe height. In practice, such height is difficult to adjust and, in most cases, the probe is not completely vertical, which impairs the reflection coefficient. Alternative feeding mechanisms, such as a disk-loaded probe, might be considered to enhance robustness against fabrication inaccuracies. Notwithstanding the above, the RLSA matching is quite satisfactory considering the extremely simple feeding mechanism, far below the usual -10 dB threshold.

The radiation performance of the RLSA prototype has been measured in an anechoic chamber by sampling the field across a complete sphere and applying near-to-far field transformation. Firstly, the measured boresight axial ratio versus frequency is plotted in Fig. 19. Despite the experimental values are not as low as those given by simulation, the axial ratio remains below 0.6 dB within a wide frequency band. Such good performance confirms the excellent polarization purity of circularly-polarized RLSA antennas.

Normalized radiation patterns at the design frequency are represented in Fig. 20 along both main planes. A very good
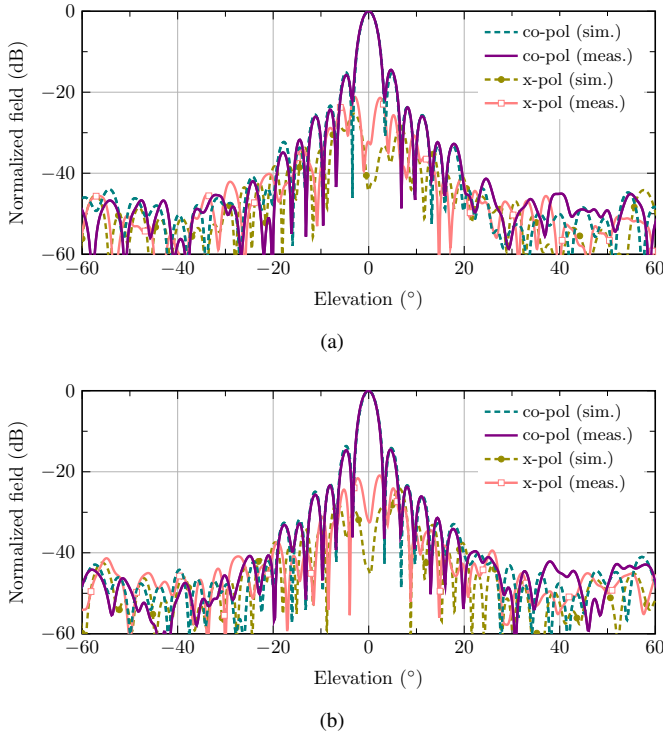
Fig. 20. Measured and simulated radiation pattern at 30 GHz: (a) $\phi = 0°$, and (b) $\phi = 90°$.

Fig. 21. Measured copolar radiation patterns at equispaced frequencies: (a) $\phi = 0°$, and (b) $\phi = 90°$.

match is observed between measurement and simulation for the directive copolar pattern, being very similar to that radiated by an ideal uniform circular aperture. Regarding crosspolar pattern, it exhibits a expected minimum at broadside direction, though not as deep as that predicted by simulation. The maximum crosspolar radiation, however, keeps below -20 dB within the whole visible range. Lastly, measured copolar radiation patterns for five equispaced frequencies within the antenna bandwidth are plotted in Fig. 21. A good frequency stability in pattern shape is evidenced, suffering the common effects of sidelobe raise and null filling as the frequency deviates from the design value.

The maximum directivity has been evaluated by integrating the measured radiation patterns over the entire sampling sphere. These values are plotted in black dots in Fig. 22 together with the simulated curve. The aperture efficiency thresholds are also shown in dashed gray to assess the illumination property. As can be seen, a very slight frequency shift can be noticed between simulation and measurement, due to fabrication tolerances. Such shift is estimated to be around 100 MHz, i.e. a small deviation of 0.3%. The measured peak directivity is 35.3 dBi, which corresponds to a remarkable value of aperture efficiency of 87% (89% in simulation). Lastly, the 1-dB-drop directivity bandwidth is 1.05 GHz, quite reasonable considering the antenna size and the series feeding of this kind of antennas.

To conclude the experimental validation, the antenna gain is evaluated by comparison with a standard LP horn in both polarizations. The measured total gain is represented in Fig. 23, where the thresholds now indicate the total efficiency.
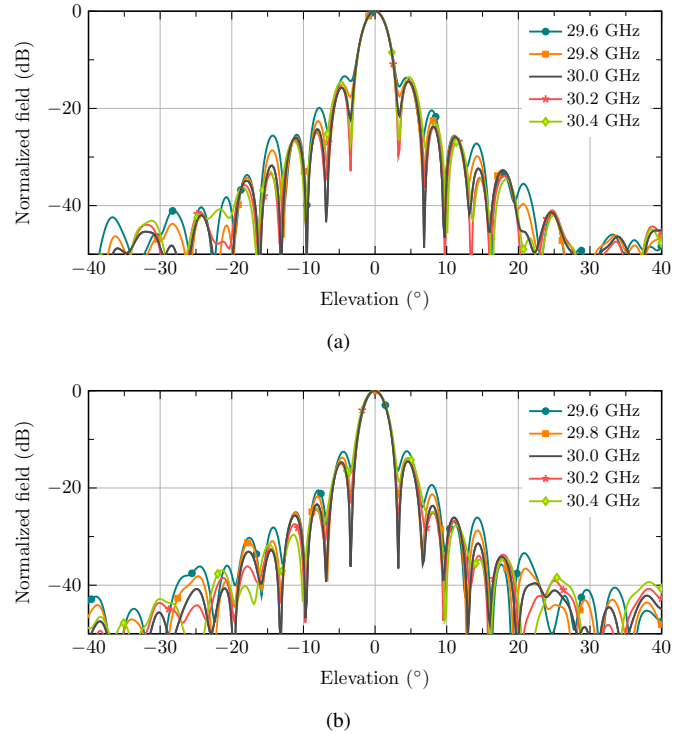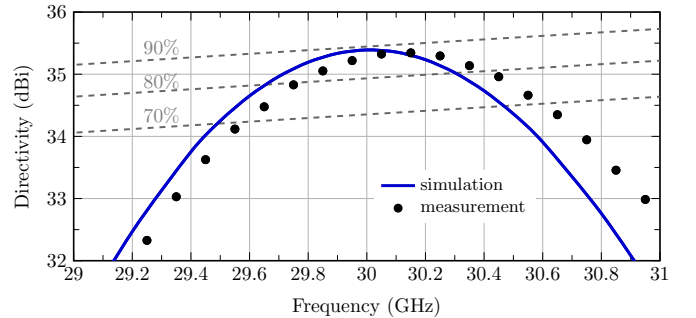

Fig. 22. Measured and simulated maximum directivity versus frequency. Aperture efficiency thresholds are indicated in dashed gray.

The maximum gain is 35.0 dBi at 30 GHz, for a peak total efficiency of 82%, outperforming the previous RLSA realizations at this frequency band. In this regard, the all-metal nature of the proposed antenna allows achieving a measured radiation efficiency of 94% at 30 GHz.

In order to assess the relevance of the proposed antenna, the main characteristics of previous CP-RLSA arrays are summarized in Table II and compared to this work. In the classical design of a dielectric-filled RLSA, a total efficiency as high as 84% was reached at 12 GHz band [14]. When such architecture is employed at higher frequencies, however, the total efficiency drops to 55% due to higher dielectric losses [15]. All-metal RLSA realizations potentially enhance the radiation efficiency as well as the power handling capability. In works [16], [17], all-metal double-layered RLSAs with corrugations are proposed for HPM applications. In these cases, however, the slot layout is not optimized, thus limiting the total efficiency

TABLE II
CP-RLSA PERFORMANCE COMPARISON

Ref.	Topology	Slow-wave mechanism	Frequency	Diameter	Gain	η_{ap}*	η_{rad}*	η_{tot}*
[14]	Single-Layer	Homogeneous dielectric	12 GHz	24 cm	28.6 dBi	n.a.	n.a.	84%
[15]	Single-Layer	Homogeneous dielectric	60 GHz	10 cm	33.4 dBi	n.a.	n.a.	55%
[16]	Double-Layer	Corrugations (all-metal)	9.5 GHz	54 cm	29.0 dBi	45%**	62%	28%
[17]	Double-Layer	Corrugations (all-metal)	12 GHz	40 cm	32.0 dBi	63%**	n.a.	63%**
[18]	Single-Layer	–	20 GHz	40.5 cm	35.9 dBi	56%	96%	54%
This work	Single-Layer	Bed of nails (all-metal)	30 GHz	20 cm	35.0 dBi	87%	94%	82%

* The aperture efficiency is measured as $\eta_{ap} = D/D_{std}$, being D the antenna maximum directivity and D_{std} the standard directivity, defined as the directivity of an ideal uniform aperture of the same area. The radiation efficiency, η_{rad}, is the ratio of the total radiated power to the net power accepted by the antenna. The total efficiency, η_{tot}, is the product $\eta_{ap} \times \eta_{rad}$, also computed as $\eta_{tot} = G/D_{std}$, being G the antenna maximum gain.
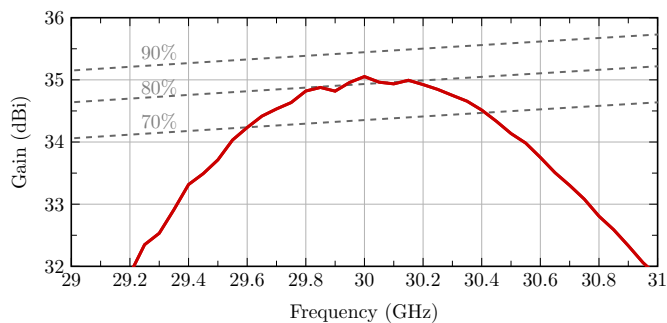** Simulated result (measurement not available).

Fig. 23. Measured and simulated gain versus frequency. Total efficiency thresholds are indicated in dashed gray.

up to 63% (in simulation) at 12 GHz. Finally, a simpler all-metal single-layer RLSA without slow-wave structure [18] is not able to reach high aperture efficiencies, remaining at 54% total efficiency at 20 GHz. In this work, an outstanding 82% of total efficiency is achieved at 30 GHz by combining an all-metal slow-wave structure and an accurate optimization process, clearly improving preceding high-frequency RLSA antennas.

VI. CONCLUSIONS

This paper presents a single-layer RLSA antenna with an all-metal slow-wave structure with the aim of maximizing the radiation efficiency in Ka band. An equivalent model for the waveguide region permits to formulate an accurate MoM analysis and optimization routine, capable of efficiently design the entire slot layout. As a consequence, aperture efficiencies above 85% can be reached, which, together with a high radiation efficiency granted by its all-metal nature, leads to a total efficiency above 80%, unprecedented for an RLSA in the millimeter-wave band. RLSA main drawback remains being its limited radiation bandwidth, inherent to the series-feed topology.

The all-metal RLSA here proposed can be considered as an appealing alternative to high-gain slot arrays fed by intricate waveguide networks in the millimeter-wave band. This antenna provides a very pure circular polarization without the need for additional polarizers, and the feeding network is extremely simple, alleviating the required fabrication tolerances and improving the radiation efficiency. Such simplicity makes this antenna well suited to be fabricated by additive manufacturing or plastic-injection molding techniques, even more so considering the contactless assembly used in the proposed implementation.

REFERENCES

[1] M. Akbari, A. Farahbakhsh, and A. Sebak, "Ridge gap waveguide multilevel sequential feeding network for high-gain circularly polarized array antenna," *IEEE Trans. Antennas Propag.*, vol. 67, no. 1, pp. 251–259, 2019.

[2] J. Wu, Y. J. Cheng, H. B. Wang, Y. C. Zhong, D. Ma, and Y. Fan, "A wideband dual circularly polarized full-corporate waveguide array antenna fed by triple-resonant cavities," *IEEE Trans. Antennas Propag.*, vol. 65, no. 4, pp. 2135–2139, 2017.

[3] M. Ferrando-Rocher, J. I. Herranz-Herruzo, A. Valero-Nogueira, and A. Vila-Jiménez, "Single-layer circularly-polarized ka-band antenna using gap waveguide technology," *IEEE Trans. Antennas Propag.*, vol. 66, no. 8, pp. 3837–3845, 2018.

[4] L. Zhang, K. Wu, S. Wong, Y. He, P. Chu, W. Li, K. X. Wang, and S. Gao, "Wideband high-efficiency circularly polarized siw-fed s-dipole array for millimeter-wave applications," *IEEE Trans. Antennas Propag.*, vol. 68, no. 3, pp. 2422–2427, 2020.

[5] B. Feng, J. Lai, K. L. Chung, T. Y. Chen, Y. Liu, and C. Y. D. Sim, "A compact wideband circularly polarized magneto-electric dipole antenna array for 5g millimeter-wave application," *IEEE Trans. Antennas Propag.*, vol. 68, no. 9, pp. 6838–6843, 2020.

[6] J. Xu, W. Hong, Z. H. Jiang, and H. Zhang, "Low-cost millimeter-wave circularly polarized planar integrated magneto-electric dipole and its arrays with low-profile feeding structures," *IEEE Antennas Wireless Propag. Lett.*, vol. 19, no. 8, pp. 1400–1404, 2020.

[7] M. Ando, K. Sakurai, N. Goto, K. Arimura, and Y. Ito, "A radial line slot antenna for 12 ghz satellite tv reception," *IEEE Trans. Antennas Propag.*, vol. 33, no. 12, pp. 1347–1353, 1985.

[8] M. Takahashi, J. Takada, M. Ando, and N. Goto, "A slot design for uniform aperture field distribution in single-layered radial line slot antennas," *IEEE Trans. Antennas Propag.*, vol. 39, no. 7, pp. 954–959, 1991.

[9] M. N. Y. Koli, M. U. Afzal, and K. P. Esselle, "Significant bandwidth enhancement of radial-line slot array antennas using a radially nonuniform tem waveguide," *IEEE Trans. Antennas and Propag.*, vol. 69, no. 6, pp. 3193–3203, 2021.

[10] M. N. Y. Koli, M. U. Afzal, K. P. Esselle, and R. M. Hashmi, "A radial line slot-array antenna with low side lobes and a uniform-phase, tapered-amplitude aperture field distribution," *IEEE Access*, vol. 8, pp. 208 532–208 542, 2020.

[11] X. Xu, A. Mazzinghi, A. Freni, and J. Hirokawa, "Simultaneous generation of three oam modes by using a rlsa fed by a waveguide circuit for 60 ghz-band radiative near-field region oam multiplexing," *IEEE Transactions on Antennas and Propagation*, vol. 69, no. 3, pp. 1249–1259, 2021.

[12] D. Comite, G. Valerio, M. Albani, A. Galli, M. Casaletti, and M. Ettorre, "Exciting vorticity through higher order bessel beams with a radial-line slot-array antenna," *IEEE Transactions on Antennas and Propagation*, vol. 65, no. 4, pp. 2123–2128, 2017.

[13] J. L. Vazquez-Roy, A. Tamayo-Domínguez, E. Rajo-Iglesias, and M. Sierra-Castañer, "Radial line slot antenna design with groove gap waveguide feed for monopulse radar systems," *IEEE Trans. Antennas Propag.*, vol. 67, no. 10, pp. 6317–6324, 2019.

[14] A. Akiyama, T. Yamamoto, M. Ando, and N. Goto, "Numerical optimisation of slot parameters for a concentric array radial line slot antenna," *IEE Proceedings-Microwaves, Antennas and Propagation*, vol. 145, no. 2, pp. 141–146, 1998.

[15] A. Akiyama, T. Yamamoto, J. Hirokawa, M. Ando, E. Takeda, and Y. Arai, "High gain radial line slot antennas for millimetre wave applications," *IEE Proceedings-Microwaves, Antennas and Propagation*, vol. 147, no. 2, pp. 134–138, 2000.

[16] C. Yuan, S. Peng, T. Shu, Z. Li, and H. Wang, "Designs and experiments of a novel radial line slot antenna for high-power microwave application," *IEEE Trans. Antennas Propag.*, vol. 61, no. 10, pp. 4940–4946, 2013.

[17] S. Peng, C. Yuan, T. Shu, J. Ju, and Q. Zhang, "Design of a concentric array radial line slot antenna for high-power microwave application," *IEEE Plasma Sci.*, vol. 43, no. 10, pp. 3527–3529, 2015.

[18] M. N. Y. Koli, M. U. Afzal, K. P. Esselle, and R. M. Hashmi, "An all-metal high-gain radial-line slot-array antenna for low-cost satellite communication systems," *IEEE Access*, vol. 8, pp. 139 422–139 432, 2020.

[19] C. D. Diallo, E. Girard, H. Legay, and R. Sauleau, "All-metal ku-band luneburg lens antenna based on variable parallel plate spacing fakir bed of nails," in *2017 11th European Conference on Antennas and Propagation (EUCAP)*, 2017, pp. 1401–1404.

[20] L. Wang, J. L. Gómez-Tornero, E. Rajo-Iglesias, and O. Quevedo-Teruel, "Low-dispersive leaky-wave antenna integrated in groove gap waveguide technology," *IEEE Trans. Antennas and Propag.*, vol. 66, no. 11, pp. 5727–5736, 2018.

[21] J. I. Herranz-Herruzo, A. Valero-Nogueira, and M. Ferrando-Bataller, "Optimization technique for linearly polarized radial-line slot-array antennas using the multiple sweep method of moments," *IEEE Trans. Antennas Propag.*, vol. 52, no. 4, pp. 1015–1023, 2004.

[22] J. I. Herranz, A. Valero-Nogueira, F. Vico, and V. M. Rodrigo, "Optimization of beam-tilted linearly polarized radial-line slot-array antennas," *IEEE Antennas Wireless Propag. Lett.*, vol. 9, pp. 1165–1168, 2010.

[23] M. Albani, A. Mazzinghi, and A. Freni, "Automatic design of cp-rlsa antennas," *IEEE Trans. Antennas Propag.*, vol. 60, no. 12, pp. 5538–5547, 2012.

[24] D. Systemes, "Cst microwave studio," *Available at: http://www.cst.com [Accessed: 20 April 2021]*, 2020.

[25] R. F. Harrington, *Time-harmonic electromagnetic fields*. McGraw-Hill, 1961.

[26] P. Kildal, E. Alfonso, A. Valero-Nogueira, and E. Rajo-Iglesias, "Local metamaterial-based waveguides in gaps between parallel metal plates," *IEEE Antennas Wireless Propag. Lett.*, vol. 8, pp. 84–87, 2009.